Magnetic properties of the quasi-XY Shastry-Sutherland magnet $Er_2Be_2SiO_7$

A. Brassington,[1] Q. Ma,[2] G. Sala,[3] A. I. Kolesnikov,[2] K. M. Taddei,[2] Y. Wu,[2] E. S. Choi,[4] H. Wang,[5] W. Xie,[5] J. Ma,[6] H. D. Zhou,[1,*] and A. A. Aczel[2,†]

[1]*Department of Physics and Astronomy, University of Tennessee, Knoxville, Tennessee 37996, USA*
[2]*Neutron Scattering Division, Oak Ridge National Laboratory, Oak Ridge, Tennessee 37831, USA*
[3]*Oak Ridge National Laboratory, Oak Ridge, Tennessee 37831, USA*
[4]*National High Magnetic Field Laboratory and Department of Physics, Florida State University, Tallahassee, Florida 32310, USA*
[5]*Department of Chemistry, Michigan State University, East Lansing, Michigan 48824, USA*
[6]*Key Laboratory of Artificial Structures and Quantum Control, Shenyang National Laboratory for Materials Science, Shanghai Jiao Tong University, Shanghai 200240, China*

(Received 13 May 2024; accepted 12 August 2024; published 10 September 2024)

Polycrystalline and single-crystal samples of the insulating Shastry-Sutherland compound $Er_2Be_2SiO_7$ were synthesized via a solid-state reaction and the floating zone method, respectively. The crystal structure, Er single-ion anisotropy, zero-field magnetic ground state, and magnetic phase diagrams along high-symmetry crystallographic directions were investigated with bulk measurement techniques, x-ray and neutron diffraction, and neutron spectroscopy. We establish that $Er_2Be_2SiO_7$ crystallizes in a tetragonal space group with planes of orthogonal Er dimers and a strong preference for the Er moments to lie in the local plane perpendicular to each dimer bond. We also find that this system has a noncollinear ordered ground state in zero field with a transition temperature of 0.841 K consisting of antiferromagnetic dimers and in-plane moments. Finally, we mapped out the H-T phase diagrams for $Er_2Be_2SiO_7$ along the directions $H \parallel [001]$, [100], and [110]. While an increasing in-plane field simply induces a phase transition to a field-polarized phase, we identify three metamagnetic transitions in the $H \parallel [001]$ case. Single-crystal neutron diffraction results reveal that the $H \parallel [001]$ phase diagram can be explained predominantly by the expected field-induced behavior of classical, anisotropic moments, although the microscopic origin of one phase requires further investigation.

DOI: 10.1103/PhysRevMaterials.8.094001

I. INTRODUCTION

Magnetic systems with a combination of geometric frustration and antiferromagnetic exchange interactions have attracted significant attention as candidates for hosting novel magnetic states with intrinsically quantum mechanical properties [1–4]. In such frustrated magnets competing exchange interactions prevent the system from finding a global arrangement of spins which minimizes energy. This suppression of long-range magnetic order allows for the formation of novel phases such as quantum spin liquids (QSLs) [5–13] characterized by long-range entanglement and capable of hosting exotic quasiparticle excitations. Frustrated magnets tend to have complicated magnetic phase diagrams with a variety of different states stabilized for various combinations of applied magnetic field and temperature. Notable examples of frustrated geometries include the kagome [14], pyrochlore [15,16], and triangular lattices [17].

The geometrically frustrated, quasi-two-dimensional Shastry-Sutherland lattice (SSL) is unique due to its realization of a magnetic Hamiltonian that is exactly solvable [18]. One can generate the SSL by starting with a square lattice and then adding an additional diagonal bond to each ion. This results in a structure where each site has one nearest neighbor (NN) with coupling strength J and four next-nearest neighbors each with coupling strength J'. Critically, the magnetic ground state of SSL systems depends both on the effective spin of the magnetic ion and the ratio J'/J [18]. For the effective spin-1/2 case with antiferromagnetic exchange interactions, when J'/J is small the ground state is known to be a product of dimer singlets. When J'/J is large, the ground state is the same antiferromagnetic Néel spin configuration expected for a simple square lattice.

The small J'/J limit is exemplified by the well-studied insulating compound $SrCu_2(BO_3)_2$ whose low-temperature ground state consists of a series of spin-singlet dimers [19,20]. Furthermore, $SrCu_2(BO_3)_2$ is close to the critical J'/J value, and it can be driven across the quantum phase transition into an antiferromagnetic Néel state by the application of pressure [21–23]. At pressures between these two extremes an intermediate singlet plaquette phase whose basic unit consists of four entangled spins is observed and multiple theoretical studies predict the existence of another intermediate QSL phase [24,25]. Under extreme magnetic fields $SrCu_2(BO_3)_2$ displays several magnetization plateaus at rational fractions of the saturation magnetization, which are attributed to the crystallization of the excited triplets [26–29]. Overall, $SrCu_2(BO_3)_2$

*Contact author: hzhou10@utk.edu
†Contact author: aczelaa@ornl.gov

provides a rich platform for exploring several novel and exotic magnetic phenomena.

Since $SrCu_2(BO_3)_2$ is a particularly fascinating system and theoretical work on the SSL abounds, there is significant interest in identifying and characterizing other magnetic materials that realize the $J'-J$ $S=1/2$ SSL model. Rare-earth-based materials are particularly attractive because crystal field effects often generate $J_{\rm eff}=1/2$ moments with a variety of magnetic anisotropies. The RB_4 (R = rare earth) family was the first group of materials studied in this context [30–38]. However, for RB_4 the crystal field schemes are not well known, the zero-field magnetic ground states are typically ordered [32,34,36,38–45], and their metallic behavior ensures that the simple J'-J SSL model is not appropriate due to the extended nature of the RKKY exchange interactions. Similar issues were identified in subsequent metallic SSL systems with the general chemical formula R_2T_2X (T = Pd, Ge, Ni, Cu, Pt, Si, Rh, and X = Mg, In, Cd, Sn, Pb, Al) [46–59].

More recently, insulating SSL systems based on rare-earth ions have been discovered. One such family is BaR_2MX_5 (M = Zn, Pd, Pt, Co; X = O, S) [60–66] and a second family is $R_2Be_2GeO_7$ [67] or $R_2Be_2SiO_7$ [68]. Limited characterization work has been reported on BaR_2MX_5, with most studies concentrating on the Nd-based systems and identifying $J_{\rm eff}=1/2$ moments, ferromagnetic dimers, and zero-field ordered ground states with predominantly in-plane spin configurations [63–65]. Interest in the $R_2Be_2GeO_7$ or $R_2Be_2SiO_7$ families is steadily increasing, with recent work describing the magnetic properties of $Tb_2Be_2Si_{1-x}Ge_xO_7$ [69], $Nd_2Be_2GeO_7$, $Pr_2Be_2GeO_7$ [70], $Er_2Be_2GeO_7$ [71], and $Yb_2Be_2GeO_7$ [72].

Here we investigate the magnetic properties of polycrystalline and single-crystal samples of $Er_2Be_2SiO_7$ with a combination of DC and AC magnetic susceptibility, magnetization, heat capacity, x-ray and neutron diffraction, and neutron spectroscopy measurements. We find that the Er moments exhibit quasi-XY magnetic anisotropy with a strong tendency to lie in the local plane perpendicular to each dimer bond. The system hosts noncollinear magnetic order with in-plane moments and antiferromagnetic dimers below 0.841 K. While an in-plane magnetic field simply polarizes the moments, an $H \parallel [001]$ field induces three metamagnetic transitions before the field-polarized phase is realized. The insulating behavior of $Er_2Be_2SiO_7$ ensures that its complex magnetic properties measured in the laboratory can be compared to theoretical predictions of the appropriate anisotropic J'-J SSL model.

II. EXPERIMENTAL METHODS

$Er_2Be_2SiO_7$ single crystals were grown using the floating zone method from a packed, phase pure polycrystalline sample with a growth speed of 10 mm/hr [68]. To synthesize the polycrystalline sample, stoichiometric amounts of Er_2O_3 (Strem Chemicals, 99.999%), SiO_2 (Alfa Aesar, 99.8%), and BeO (Alfa Aesar, 99%) were ground and packed into a long cylindrical rod. This rod was first annealed in air at 1000 °C and then twice more at 1400 °C for 20 hr each time with intermediate grindings. A similar procedure was used to synthesize polycrystalline $Lu_2Be_2SiO_7$ with Lu_2O_3 (Alfa Aesar, 99.99%) substituted for Er_2O_3.

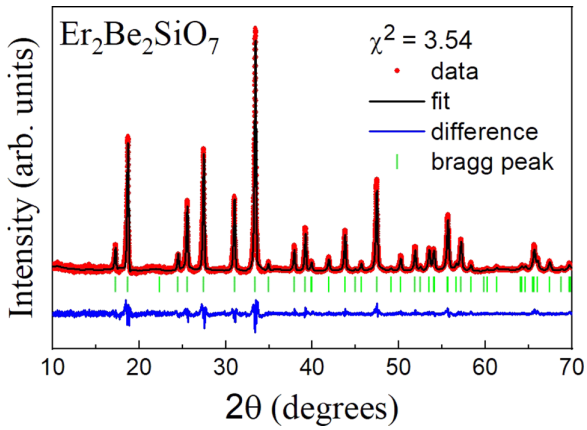

FIG. 1. Room temperature XRD pattern of $Er_2Be_2SiO_7$. The red circles represent experimental data, the black curve shows the fitted pattern, the blue line depicts the difference curve, and the green ticks indicate Bragg positions.

The phase purity of both the powders and single crystals was confirmed by performing room temperature powder x-ray diffraction (XRD) using a HUBER imaging plate Guinier camera 670 with Cu radiation ($\lambda = 1.54059$ Å). The single-crystal samples were first crushed for these measurements. Refinement of the XRD patterns were done with the software package FULLPROF [73] using the structure of $Y_2Be_2SiO_7$ [74] as a starting reference. The refined powder diffraction pattern for the $Er_2Be_2SiO_7$ powder is shown in Fig. 1. Single-crystal x-ray diffraction (SXRD) measurements were carried out on a Bruker Eco Quest X-ray Diffractometer using Mo radiation ($\lambda = 0.71073$ Å) at 300 K, and the refinement was done using the Bruker SHELXTL software package. The main results are presented in Table I, and the results agree well with the previous powder refinement [68]. For all directional-dependent measurements, the crystal orientation was determined using the Laue backscattering method.

Temperature- and field-dependent magnetization data were collected at the University of Tennessee using a Materials Property Measurement System (MPMS) from Quantum Design with a vibrating squid magnetometer (VSM) option. Magnetization measurements at He-3 temperatures were carried out in the same MPMS using a He-3 insert also from Quantum Design. Heat capacity measurements under field were carried out using a Physical Property Measurement System (PPMS) Dynacool with a He-3 insert at Shenyang National Laboratory. AC susceptibility measurements were

TABLE I. Atomic coordinates and isotropic displacement parameters $U_{\rm eq}$ (Å^2). All sites are fully occupied.

Atom	Wyck.	x	y	z	$U_{\rm eq}$
Er	4e	0.15907(3)	0.65907(3)	0.50719(8)	0.0041(19)
Si	2a	0	0	0	0.0036(5)
Be	4e	0.6352(14)	0.1352(14)	0.960(3)	0.0060(18)
O_1	2c	0	1/2	0.180(2)	0.0069(17)
O_2	4e	0.6411(7)	0.1411(7)	0.2934(5)	0.0041(11)
O_3	8f	0.0816(8)	0.1634(7)	0.2017(10)	0.0050(8)

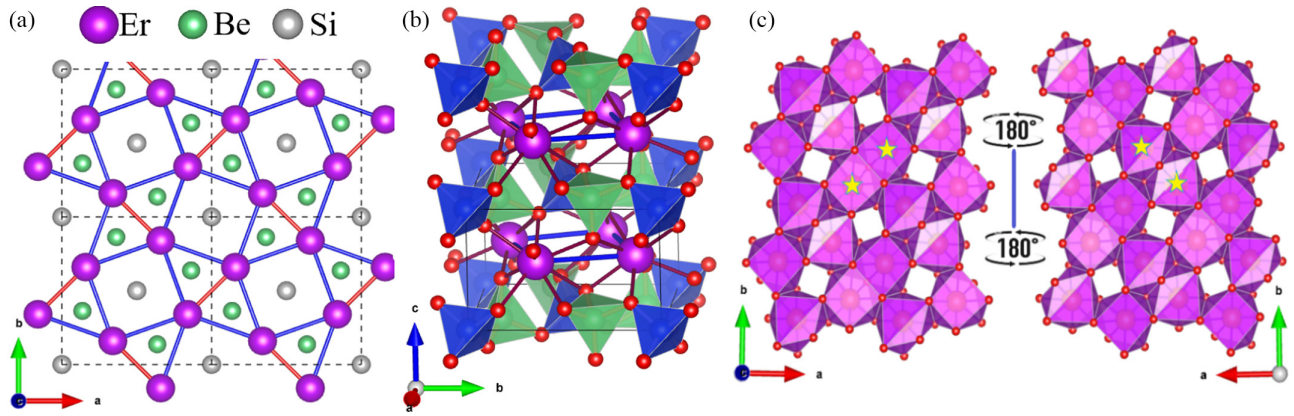

FIG. 2. (a) Schematic diagram of the Er^{3+} ions forming a SSL lattice in the *ab* plane. Intradimer bonds J (3.265 Å) are shown in red and interdimer bonds J' (3.862 Å) in blue. The relative positions of the Be and Si ions are also shown. (b) Structure of $Er_2Be_2SiO_7$ viewed slightly off the [100] axis. The SSL layers formed by the ErO_8 polyhedra are separated by layers of BeO_4 (green) and SiO_4 (blue) tetrahedra. (c) The monoclinic point symmetry (C_s) of the Er ions is best illustrated by viewing the crystal structure along the [001] and [00-1] directions. A single NN pair of Er ions is marked with stars for reference. The normal to the mirror plane lies along the crystallographic [110] or [1-10] direction for the orthogonal dimer sublattices in the system.

performed at the National High Magnetic Field Laboratory (NHMFL) with both He-3 and dilution refrigerator configurations.

Neutron powder diffraction was performed using the high-resolution HB-2A powder diffractometer [75] at the High Flux Isotope Reactor (HFIR) of Oak Ridge National Laboratory (ORNL). The ∼4 g powder sample was sealed inside an aluminum can with 1 atm of helium exchange gas. Diffraction patterns were measured at 280 mK and 4 K with a wavelength of 2.41 Å and a collimation of open-open-12′. Inelastic neutron scattering on ∼3 g of similarly prepared powder was performed on the direct geometry time-of-flight chopper spectrometer SEQUOIA [76] at the Spallation Neutron Source (SNS) at ORNL. Data were collected at 5 and 25 K with incident energies of 25 and 80 meV. For these measurements, the fine Fermi chopper was spun at 240 or 480 Hz, and the T_0 chopper setting was 60 or 90 Hz. Spectra were collected with the same instrument settings on a similar mass of the nonmagnetic reference sample $Lu_2Be_2SiO_7$ to facilitate a background subtraction of the phonon spectra.

A single-crystal neutron diffraction experiment was performed on the DEMAND (HB-3A) beamline [77] at the HFIR with an incident wavelength of 1.542 Å. A single-crystal sample with a mass ∼30 mg was measured in two-axis mode in a vertical-field cryomagnet down to temperatures of 280 mK using a He-3 insert. A magnetic field of up to 2 T was applied along the [001] axis.

III. RESULTS AND DISCUSSION

A. Crystal structure

$Er_2Be_2SiO_7$, like all members of the $R_2Be_2SiO_7$ family, crystallizes into a tetragonal lattice with space group $P-42_1m$ (113). The room-temperature lattice constants determined via single-crystal XRD are $a = 7.2572(4)$ Å and $c = 4.7396(3)$ Å. The structure consists of planes of eightfold coordinated Er^{3+} ions with spacer layers containing both Si-O and Be-O tetrahedra. The sublattices formed by Er, Be, and Si all stack in an AAA-type fashion along the [001] axis. The magnetic Er^{3+} and nonmagnetic Be^{2+} ions both form SSLs in plane, while the nonmagnetic Si^{4+} ions form a square lattice. The NN and NNN in-plane distances at room temperature are 3.265 Å and 3.862 Å, respectively, while the shortest interplane distance is 4.740 Å, which implies a quasi-two-dimensional magnetic system. Schematics of the crystal structure viewed along the [001] axis and just slightly off the *a* axis are shown in Figs. 2(a) and 2(b), with an outline of the chemical unit cell also shown in the latter.

The Er and Be ions occupy two different 4*e* Wyckoff sites, while Si occupies the 2*a* Wyckoff site. The ligand environment around the Er^{3+} ions are irregularly shaped polyhedra consisting of eight O^{2-} ions, as shown in Fig. 2(c). Opposite faces of the polyhedra, located above and below the SSL planes, have distorted square and diamond geometries, respectively. The Er^{3+} ions have a monoclinic point group symmetry of C_s, which means that their only symmetry element is a mirror plane. The Er ions forming the two different types of dimers have different directions for their mirror plane normals corresponding to the crystallographic [110] and [1-10] axes. The ErO_8 polyhedron shares a face with its one NN polyhedron and an edge with each of its four NNN polyhedra. Detailed crystal structure refinement results obtained from single-crystal XRD are given in Table I. An image of a floating zone crystal boule and a Laue pattern with the beam oriented along the crystallographic [001] axis are shown in Fig. 3.

B. Single-ion anisotropy and crystal fields

Figure 4 shows the T dependence of both the magnetic susceptibility χ (plotted as M/H) and its inverse $1/\chi$ along three high-symmetry crystallographic directions. $1/\chi$ does not have a linear T dependence throughout the entire range measured due to the increased depopulation of excited Er^{3+} crystal field levels with decreasing temperature. The $1/\chi$ data were first fitted to a Curie-Weiss law in the high-temperature range 150–300 K, and we found that the Er^{3+} effective moment agrees well with expectations for a free ion system, with a small variation for the different datasets. The values

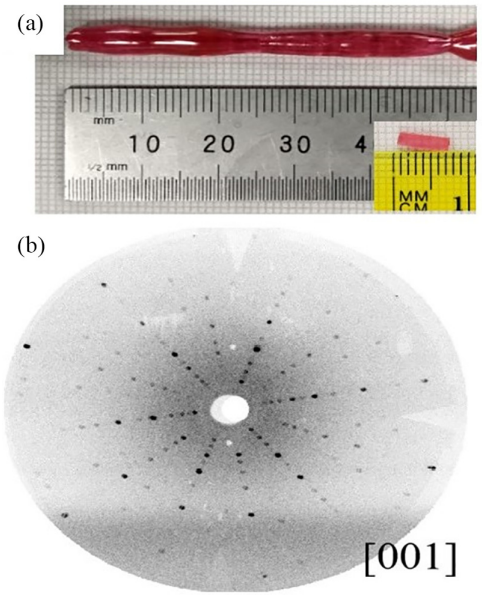

FIG. 3. (a) An as-grown crystal boule of $Er_2Be_2SiO_7$. (b) The Laue pattern generated with the incident x-ray beam along the crystallographic [001] axis.

were 9.3597(4) μ_B for $H \parallel [001]$, 9.4618(2) μ_B for $H \parallel [110]$, and 9.6158(2) μ_B for $H \parallel [100]$. Using the same fit range the Curie-Weiss (θ_{cw}) temperatures obtained for each direction are 16.30(6) K for $H \parallel [001]$, −25.76(4) K for $H \parallel [110]$, and −41.64(3) K for $H \parallel [100]$. We proceeded to perform another fit to the same Curie-Weiss function in the low-temperature range 2–6 K. The Curie-Weiss temperatures θ_{cw} are negative for all three datasets, with values of −4.29(4) K for $H \parallel [001]$, −2.15(3) K for $H \parallel [110]$, and −1.77(3) K for $H \parallel [100]$. The effective moments obtained using the low-temperature fit range are 9.649(5) K for $H \parallel [001]$, 7.630(3) K for $H \parallel [110]$, and 7.276(3) K for $H \parallel [100]$. The sign of θ_{CW} indicates that $Er_2Be_2SiO_7$ has dominant antiferromagnetic exchange interactions, which is likely due to an antiferromagnetic intradimer coupling.

Figure 5(a) shows DC magnetization vs applied field at 2 K. Interestingly, the saturation magnetization ratio between the [110] and [100] directions, $M_{sat}^{110}/M_{sat}^{100}$, is almost exactly $\sin(45^\circ) = 1/\sqrt{2}$. This observation can be used to draw some general conclusions about the Er^{3+} single-ion anisotropy in this system. Since the SSL can be described as two interpenetrating square networks of orthogonal dimers, the measured anisotropy in the *ab*-plane magnetization can arise from a combination of a [110] easy axis and a [1-10] hard axis for one dimer sublattice and vice versa for the second dimer sublattice. A [110] applied field would then polarize only one sublattice while the other would not respond to it at all. For a [100] applied field, both sublattices would contribute to the field-polarized state in an equivalent manner, as all moments would have a component along the field direction but they would remain parallel to their local [110] easy-axis direction. Schematics of the expected field-polarized states for the [100] and [110] applied field directions that are consistent with the anisotropic saturation magnetization values are shown in Figs. 5(b) and 5(c). Similar in-plane anisotropy has been observed in other magnetic systems with a SSL geometry, including Yb_2Pt_2Pb [55] and $BaNd_2ZnS_5$ [64].

The saturation magnetization ratio of $M_{sat}^{110}/M_{sat}^{001} \approx 1/2$ provides additional insight into the Er^{3+} single-ion anisotropy. Based on the established *ab*-plane anisotropy, the [001] saturation magnetization can be explained by a simple field-polarized state with the moments from both sublattices aligned with the field. Since the low-field magnetization slopes are nearly equivalent for the [110] and [001] field directions when scaling the former dataset to account for the decreased number of moments contributing to the response, $Er_2Be_2SiO_7$ appears to be an XY (or quasi-XY) magnet. This behavior differs strongly from observations for Yb_2Pt_2Pb [59,78] and $BaNd_2ZnS_5$ [64], where the *c* axis turned out to be a hard direction for the magnetization.

To investigate quantitative details of the magnetic anisotropy induced by crystal fields, inelastic neutron scattering (INS) measurements on a polycrystalline sample of $Er_2Be_2SiO_7$ were conducted using the time-of-flight chopper spectrometer SEQUOIA. Datasets were collected with incident energies of 25 meV and 80 meV at temperatures of 5 and 25 K to measure the crystal field levels associated with the $J = 15/2$ ground state multiplet of Er^{3+} and the virtual

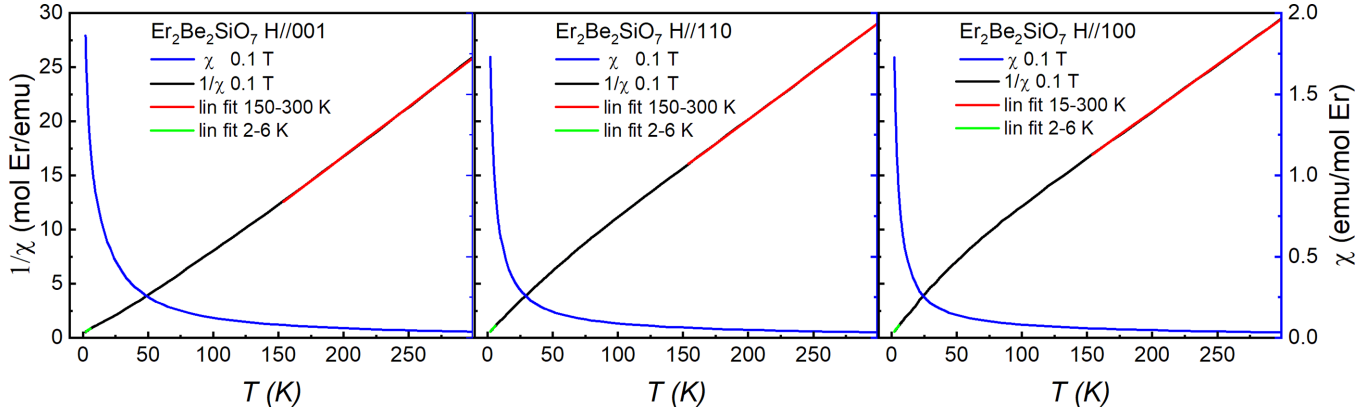

FIG. 4. $1/\chi$ (left) and χ (right) vs T for $H \parallel [001]$, $H \parallel [110]$, and $H \parallel [100]$ collected at 0.1 T. Linear fits are performed between 150–300 K and 2–6 K. The obtained θ_{cw} and μ_{eff} values are noted in the text.

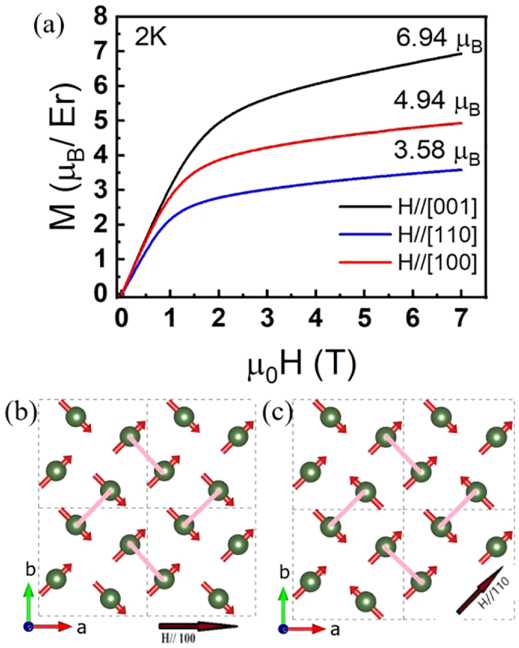

FIG. 5. (a) DC magnetization (M) vs field (H) for the three high-symmetry directions $H \parallel [001]$, $H \parallel [100]$, and $H \parallel [110]$. The magnetization values at 7 T are provided in the panel. (b) Predicted field-polarized spin structure for $H \parallel [100]$. The moments are confined to the *ab* plane and make a 45° angle with the local [100] axis. (c) Predicted field-polarized spin structure for $H \parallel [110]$. Due to in-plane anisotropy with a strong tendency for the moments to point along local [110] directions, only one sublattice is polarized while the other one is essentially unresponsive.

transitions created by thermally populating the lowest-lying crystal field level. Er^{3+} is a Kramers ion, so the crystal field ground state must be at least two-fold degenerate. As shown in Figs. 2(b) and 2(c), each Er ion is surrounded by eight oxygen ions that generate a monoclinic C_s environment. The low symmetry of this point group is expected to produce maximal splitting of the 16 levels associated with the $J = 15/2$ ground state multiplet, so up to seven excited crystal field doublets may be visible in the low-temperature INS data.

Figures 6(a) and 6(b) present color contour plots of the $E_i = 25$ meV and 80 meV datasets, respectively, at 5 K. The phonon spectra from a nonmagnetic reference sample of $Lu_2Be_2SiO_7$ were subtracted off from these data. There are three strong, flat modes in the lower incident energy dataset centered about energy transfers of 1.75 meV, 5.22 meV, and 13.73 meV, with two additional strong modes visible in the other dataset centered about energy transfers of 22.54 meV and 27.87 meV. Three weaker modes are also present at energy transfers of 3.47 meV, 7.12 meV, and 49.46 meV. All eight modes have a magnetic origin, as their intensities decrease monotonically with increasing Q. The higher temperature data collected at 25 K is shown in Figs. 6(c) and 6(d) and proved invaluable for elucidating the crystal field scheme. While seven of the eight modes previously observed had reduced intensity at 25 K, the intensity of the 3.47 meV mode was enhanced. This finding suggests that this mode corresponds to a virtual crystal field transition. Indeed, the energy of this mode corresponds to the difference between the first and second excited doublets. Therefore, the other seven levels observed at 5 K are the expected transitions associated with the ground state doublet. Several other virtual crystal field transitions are observed in the 25 K datasets as well, with the most prominent features centered at 8.51 meV and 11.98 meV. The energy levels and integrated intensities of these CEF excitations have been extracted by fitting constant Q cuts (integration range of 1.5 to 2 $Å^{-1}$ and 3 to 3.5 $Å^{-1}$ for the $E_i = 25$ meV and 80 meV datasets respectively) to a sum of Lorentzian functions with a linear background. The integrated intensities of the crystal field modes above 20 meV were normalized by a scale factor obtained by comparing the integrated intensities of the 13.73 meV mode in both the low- and high-incident energy datasets.

To ensure that all the crystal field parameters are real, we choose the local y axis to be perpendicular to the mirror plane associated with the C_s point group [79,80]. As mentioned above, this corresponds to the [110] crystallographic direction for one of the dimer sublattices, and it is guaranteed to be one of the principal g-tensor directions by symmetry. On the other hand, the two principal g tensor directions in the xz plane are strongly dependent on the details of the surrounding ligands, and they are not known *a priori*. Our choice of y axis generates the following CEF Hamiltonian with 15 terms:

$$\begin{aligned}\mathcal{H} = {} & B_2^0\hat{O}_2^0 + B_2^1\hat{O}_2^1 + B_2^2\hat{O}_2^2 + B_4^0\hat{O}_4^0 + B_4^1\hat{O}_4^1 + B_4^2\hat{O}_4^2 \\ & + B_4^3\hat{O}_4^3 + B_4^4\hat{O}_4^4 + B_6^0\hat{O}_6^0 + B_6^1\hat{O}_6^1 + B_6^2\hat{O}_6^2 + B_6^3\hat{O}_6^3 \\ & + B_6^4\hat{O}_6^4 + B_6^5\hat{O}_6^5 + B_6^6\hat{O}_6^6,\end{aligned}$$

where B_n^m and $\hat{O}_n^m$ represent the crystal field parameters and the corresponding operators in Stevens notation. Note that $B_n^m = \lambda_n^m \theta_n A_n^m$, where λ_n^m are normalization constants [81], θ_n are constants associated with the electron orbitals of Er^{3+} [82,83], and A_n^m are the crystal field parameters in Wybourne notation.

The standard approach for determining crystal field parameters from INS data for higher point-symmetry systems is to perform a point charge calculation to obtain reasonable starting values and then refine the parameters through a least-squares fitting process with the data using the typical χ^2 minimization function. For an under-constrained problem with a low point symmetry such as the present case, there is a strong likelihood that this procedure will not result in a meaningful solution since the fitting routine may get stuck in the same local minimum each time. To mitigate this issue and facilitate quick comparisons between INS data and crystal field models, the software package CrysFieldExplorer was developed recently [84]. One key advantage of CrysFieldExplorer is the use of a revised cost/loss function for comparing the experimental and calculated CEF energy levels, which significantly reduces the likelihood of getting stuck in local minima. CrysFieldExplorer also takes advantage of high-performance parallel computing so rapid searches through complex parameter spaces can be conducted. This allows one to bypass the crystal field point charge calculation step in the determination of crystal field parameters from INS data and set up a random parameter initialization instead so that the parameter space search is not biased towards particular local minima. Note that CrysFieldExplorer reports crystal field parameters as B_n^m/θ_n.

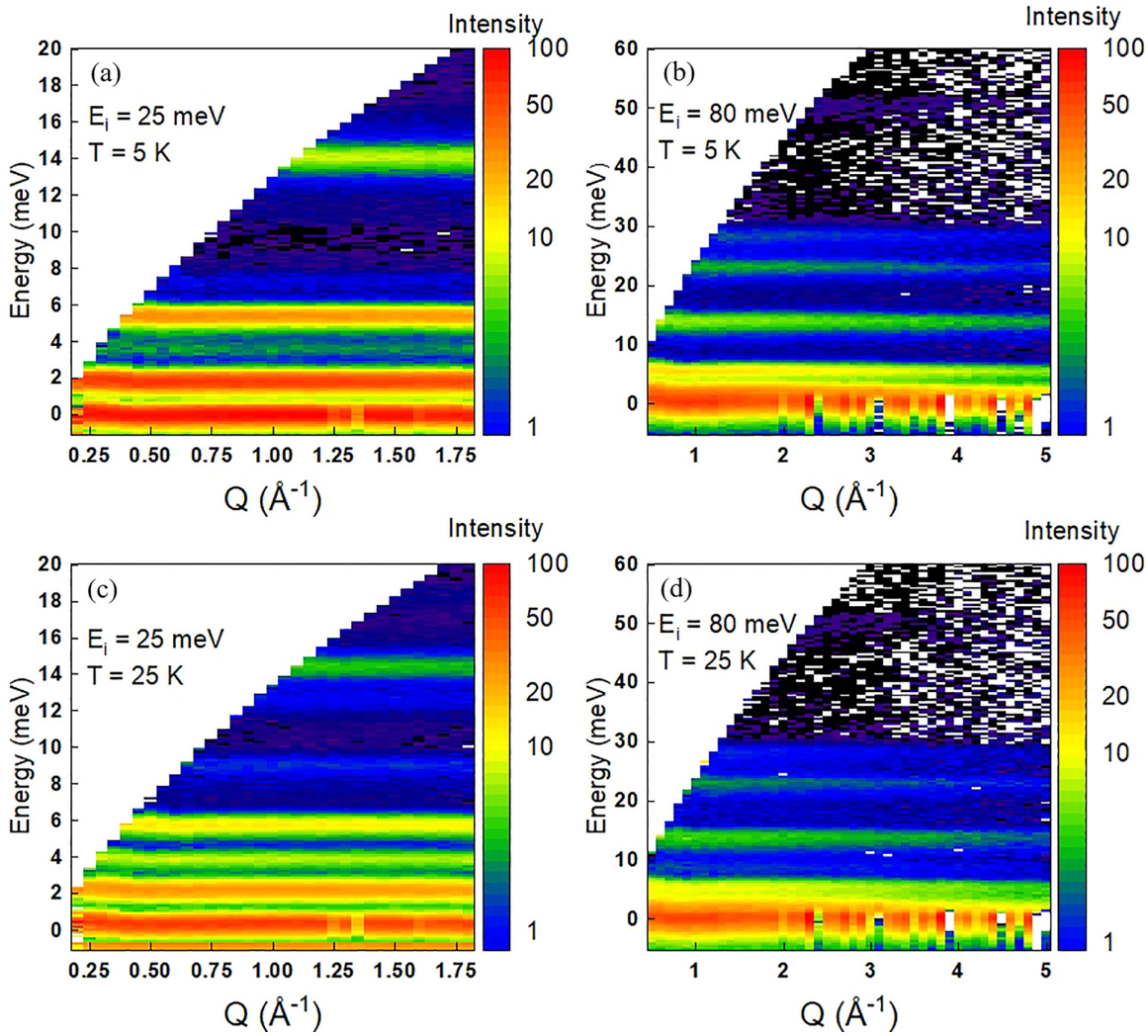

FIG. 6. Color contour plots of the scattering intensity (in arb. units) as a function of momentum transfer Q and energy transfer E for the following datasets: (a) $E_i = 25$ meV, $T = 5$ K, (b) $E_i = 80$ meV, $T = 5$ K, (c) $E_i = 25$ meV, $T = 25$ K, (d) $E_i = 80$ meV, $T = 25$ K. Several crystal field excitations from Er^{3+} are visible in this data.

Promising crystal field parameter sets for $Er_2Be_2SiO_7$ were obtained by considering a custom loss function of the form

$$L_{\text{tot}} = L_E + L_{\text{Int}} + L_M, \tag{1}$$

where L_E, L_{Int}, and L_M are the loss function components for the INS energy levels, the INS integrated intensities and the 2 K powder-averaged M vs H data respectively. Their functional forms are given by

$$L_E = \log_{10}\left(\sum_i \frac{\det\left\{\left(E_i^{\text{exp}} + E_0^{\text{cal}}\right)\mathcal{I} - \mathcal{H}\right\}^2}{\det\left\{E_i^{\text{exp}}\mathcal{I}\right\}^2}\right), \tag{2}$$

$$L_{\text{Int}} = \frac{\sqrt{\sum\left(I_i^{\text{exp}} - I_i^{\text{calc}}\right)^2}}{\sqrt{\sum\left(I_i^{\text{exp}}\right)^2}}, \tag{3}$$

$$L_M = \frac{\sqrt{\sum\left(M_i^{\text{exp}} - M_i^{\text{calc}}\right)^2}}{\sqrt{\sum\left(M_i^{\text{exp}}\right)^2}}, \tag{4}$$

where $\mathcal{I}$ represents the identity matrix, $\mathcal{H}$ is the CEF Hamiltonian, and "det" denotes the determinant of a matrix. While L_E includes contributions from the 5 K INS data only, L_{Int} includes intensities from both the 5 K and 25 K INS datasets. The summation on index i in Eq. (4) is carried out using a field interval three times larger than the measurement step size to reduce the computation time of the powder-averaged magnetization calculations.

The complete set of INS energy levels and integrated intensities included in the fitting process are presented in Table II. Due to the large crystal field parameter space, CrysFieldExplorer used the covariance matrix adaptation evolution strategy (CMA-ES) to minimize $L_E + L_{\text{Int}}$ initially. The fitting routine was run over 1900 times to sample the loss space, and 129 solutions were found that matched the INS data significantly better than other solutions. Due to the computational cost of simulating powder-averaged magnetization data, L_M was not included in the initial optimization but was later used in conjunction with the loss function from the INS data to assess the candidacy of the remaining 129 possible solutions. L_{tot} vs B_2^0/θ_2 for each of the 129 solutions is plotted in Fig. 7(a) with the chosen coordinate system for the crystal field parameters corresponding to the one with $B_2^1 = 0$, which

TABLE II. Measured CEF energy levels and the integrated intensities for all the transitions measured with INS. When the initial state corresponds to the CEF ground state doublet (i.e. 0), the data were collected at 5 K. Otherwise, the data were collected at 25 K. All the measured integrated intensities were normalized to the value for the 1.75 meV mode. The calculated integrated intensities for the two most probable CEF parameter sets discussed in the main text are also presented.

Transition	E_{obs}(meV)	I_{obs}	I_{calc1}	I_{calc2}
0-1	1.75(3)	1.0	1.0	1.0
0-2	5.22(3)	0.43(6)	0.408	0.357
0-3	7.12(5)	0.007(3)	0.020	0.029
0-4	13.73(1)	0.160(6)	0.152	0.156
0-5	22.54(5)	0.073(7)	0.047	0.078
0-6	27.87(8)	0.025(4)	0.016	0.021
0-7	49.46(11)	0.0064(9)	0.013	0.006
1-2	3.47	0.20(3)	0.192	0.227
2-4	8.51	0.040(3)	0.048	0.044
1-4	11.98	0.022(5)	0.005	0.006

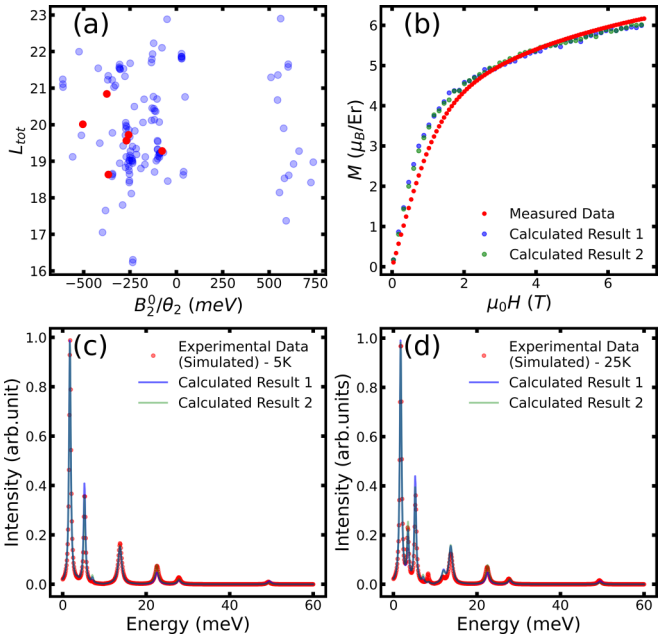

FIG. 7. (a) The loss function value vs B_2^0/θ_2 for all 129 crystal field parameter solutions determined by CrysFieldExplorer. The solid red circles represent the six unique solutions that are consistent with the known magnetic anisotropy of the system and satisfy the hard g-tensor constraints as discussed in the main text. (b) A comparison of the calculated (blue and green circles) vs measured (red circles) powder-averaged magnetization. The calculated magnetization curves for the two most probable crystal field solutions (as discussed in the main text) are shown. (c, d) A comparison of the calculated (blue and green curves) vs simulated experimental INS spectra (red circles) at 5 K and 25 K, respectively. The calculated spectra for the two most probable crystal field solutions are superimposed on the simulated data.

has often been used for this low point symmetry previously to make comparisons between different crystal field parameters more straightforward [85]. In other words, for the specific Er ion being considered here the local y axis is aligned with the crystallographic [110] direction and the x and z axes make an arbitrary angle with the crystallographic [1-10] and [001] directions, respectively. The large number of solutions with low L_{tot} values indicate that a simultaneous fit of these three datasets is insufficient to fully constrain the 15 CEF parameters for this system.

To further constrain the possible crystal field parameter solutions, we use the 2 K M vs H data shown in Fig. 5(a) to establish approximate lower and upper bounds for the g-tensor components of the crystal field ground state doublet. We note that these bounds are based on the assumption that the principal g-tensor components are along the [110], [1-10], and [001] crystallographic directions for the Er ions forming one dimer sublattice, which correspond to the y, x, and z axis in the local frame, respectively. For the second Er dimer sublattice, the in-plane crystallographic directions corresponding to the x and y axes are reversed. Although the monoclinic site symmetry of the Er ions in this system ensures that the principal directions of the g tensor in the xz plane cannot be uniquely determined by symmetry constraints, a nearest-neighbor point charge calculation of the crystal field levels suggests that they are within 20° of our assumption. A magnetic structure refinement of recent low-temperature neutron diffraction data collected on the sister compound $Dy_2Be_2SiO_7$ provides further support for this assumption, as the moment direction was found to be in the xz plane with the local x-axis (or true Ising axis) making an angle of $\sim 17°$ with the crystallographic [1-10] (or [110]) direction [86].

Subtracting off the linear van Vleck contribution for each field direction leads to saturation magnetization values of 2.65, 3.92, and 4.83 μ_B for $H \parallel$ [110], [100], and [001] respectively. As described above, the Er moments display a large anisotropy in the SSL planes, with a strong tendency to point along their local y-axis directions. This behavior suggests that g_{xx} should be small. The other interesting observation from this data is that $M_{sat}^{110}/M_{sat}^{100} \approx 1/\sqrt{2}$ and $M_{sat}^{110}/M_{sat}^{001} \approx 1/2$. Since we argued above that only one Er dimer sublattice contributes to the magnetization with a magnetic field $H \parallel$ [110] while both sublattices should contribute equally when $H \parallel$ [001], this implies that g_{yy} and g_{zz} are very similar and the system has a quasi-XY magnetic anisotropy. As we will discuss in the next section, we also find that the ordered moment points along the local y direction. Therefore, we assume that appropriate crystal field solutions should have $g_{yy} > g_{zz}$. Finally, we can place hard constraints on the maximum possible g_{yy} and g_{zz} values from the 2 K saturation magnetization (note that these are not exact g_{yy} and g_{zz} values due to the low-lying crystal field level at 1.75 meV) and the minimum possible g_{yy} value from the magnitude of the ordered moment determined from neutron diffraction. We find that the upper bounds on g_{yy} and g_{zz} are given by $4M_{sat}^{110} = 10.6$ and $2M_{sat}^{001} = 9.66$ respectively. The magnitude of the ordered moment, as determined from neutron diffraction, has a value of 2.47(3) μ_B and sets a lower limit on $g_{yy} = 4.94$.

With the hard constraints on the g-tensor components of the crystal field ground state doublet now established as $4.94 < g_{yy} < 10.6$ and $0 < g_{zz} < 9.66$, the number of viable solutions from the CrysFieldExplorer analysis described above can be

TABLE III. The crystal field parameters (in Stevens notation), the diagonal g-tensor components, and the L_{tot} values for the six unique solutions identified with CrysFieldExplorer that are consistent with the known magnetic anisotropy of the system and satisfy the hard g-tensor constraints discussed in the main text. The crystal field parameters are provided in units of meV.

B_n^m	1	2	3	4	5	6
B_2^0	-9.32×10^{-2}	-1.95×10^{-2}	-6.86×10^{-2}	-6.55×10^{-2}	-1.28×10^{-1}	-9.55×10^{-2}
B_2^1	0	0	0	0	0	0
B_2^2	1.88×10^{-1}	2.97×10^{-1}	2.53×10^{-1}	2.49×10^{-1}	2.64×10^{-1}	1.94×10^{-1}
B_4^0	4.93×10^{-5}	2.31×10^{-4}	5.33×10^{-4}	3.18×10^{-4}	1.35×10^{-4}	4.66×10^{-4}
B_4^1	-1.75×10^{-3}	-8.48×10^{-4}	4.13×10^{-3}	-3.44×10^{-3}	-3.34×10^{-5}	-2.58×10^{-3}
B_4^2	-2.20×10^{-3}	-2.66×10^{-3}	-5.46×10^{-4}	-1.03×10^{-3}	-1.82×10^{-3}	-3.21×10^{-4}
B_4^3	1.08×10^{-2}	4.20×10^{-3}	-7.33×10^{-3}	9.59×10^{-3}	1.04×10^{-2}	1.39×10^{-2}
B_4^4	3.21×10^{-3}	3.27×10^{-3}	3.17×10^{-4}	-6.70×10^{-5}	6.70×10^{-4}	3.75×10^{-4}
B_6^0	5.44×10^{-7}	-2.57×10^{-6}	-3.17×10^{-6}	-6.71×10^{-6}	1.72×10^{-6}	-2.32×10^{-6}
B_6^1	-5.84×10^{-6}	-6.56×10^{-5}	-1.24×10^{-5}	2.86×10^{-5}	1.10×10^{-5}	1.19×10^{-5}
B_6^2	2.09×10^{-5}	9.36×10^{-6}	1.43×10^{-5}	1.99×10^{-5}	2.24×10^{-6}	1.76×10^{-6}
B_6^3	-3.87×10^{-5}	6.25×10^{-6}	7.82×10^{-5}	-4.78×10^{-5}	-6.85×10^{-5}	-8.38×10^{-5}
B_6^4	-2.96×10^{-5}	-2.17×10^{-5}	-7.60×10^{-5}	8.13×10^{-7}	-4.24×10^{-5}	-1.48×10^{-5}
B_6^5	1.65×10^{-4}	4.70×10^{-5}	1.80×10^{-6}	1.50×10^{-5}	4.84×10^{-5}	1.17×10^{-4}
B_6^6	-5.49×10^{-5}	-1.31×10^{-5}	-5.22×10^{-5}	-4.18×10^{-5}	1.78×10^{-5}	3.77×10^{-5}
g_{xx}	2.57	2.33	1.72	0.03	0.57	1.49
g_{yy}	9.48	9.57	10.1	8.81	9.76	10.2
g_{zz}	6.62	7.02	6.96	8.12	7.80	7.79
L_{tot}	18.64	19.28	19.56	19.73	20.01	20.84

drastically reduced. Note that g_{xx} and g_{zz} are interchangeable here due to two degenerate sets of crystal field parameters related by a 90° rotation about the y axis that we could not differentiate between when fitting the INS data above. Taking these criteria into account drastically reduces the number of acceptable solutions from 129 to 17. Two of them can be discarded immediately due to their nearly isotropic g tensors, which are inconsistent with the known magnetic anisotropy of the system. Furthermore, only six of the remaining solutions are unique. Their B_2^0/θ_2 values are depicted with solid red circles in Fig. 7(a). Their crystal field parameters, diagonal g-tensor components, and L_{tot} values are presented in Table III in order of increasing L_{tot}. The calculated integrated intensities for the $L_{\text{tot}} = 18.64$ (I_{calc1}) and 19.28 (I_{calc2}) solutions from Table III are shown in Table II. Figure 7(b) compares the calculated M vs H to the experimental data for the same two solutions. Figures 7(c) and 7(d) show similar comparisons with the 5 K and 25 K INS data, respectively. The experimental (simulated) neutron scattering spectra were plotted here by using a sum of Lorentzian functions with the measured (calculated) energy levels, the measured (calculated) integrated intensities, and fixed widths independent of energy transfer. Both solutions successfully account for most energy levels and their relative integrated intensities, although it is difficult to capture the small feature at ∼7 meV accurately as the low intensity ensures that its contribution to L_{tot} is minimal.

C. Zero-field magnetic ground state

The magnetic susceptibility χ vs T for a 0.1 T field applied along the crystallographic [001], [110], and [100] directions is shown in Fig. 8. All three datasets show a decrease in the signal at an average temperature of 0.841 K, which is indicative of a phase transition to long-range antiferromagnetic order. The enhanced signal reduction for the in-plane directions suggests that the ordered moments lie in the SSL plane.

To determine the ordered spin configuration in the antiferromagnetic ground state, we performed neutron powder diffraction measurements. The nuclear structure was first

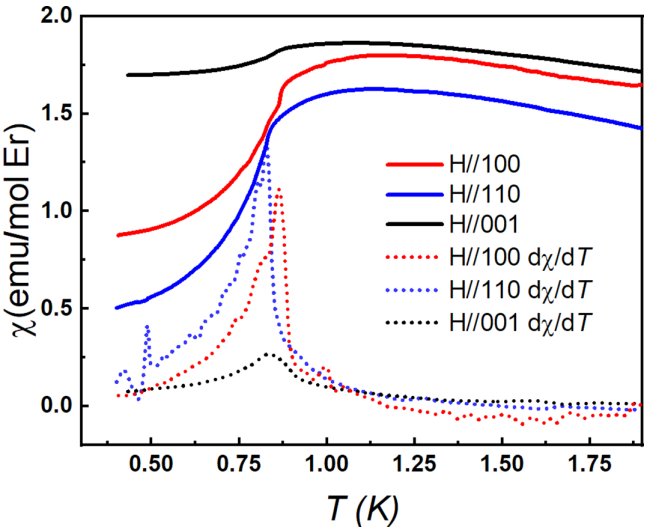

FIG. 8. The DC susceptibility (χ) and its derivative ($\mathrm{d}\chi/dT$) vs T measured at 0.1 T along three high-symmetry crystallographic directions. The peaks in ($\mathrm{d}\chi/dT$), indicative of the magnetic transition temperature, are visible at 0.832, 0.827, and 0.865 K for applied fields along the [001], [110], and [100] directions, respectively.

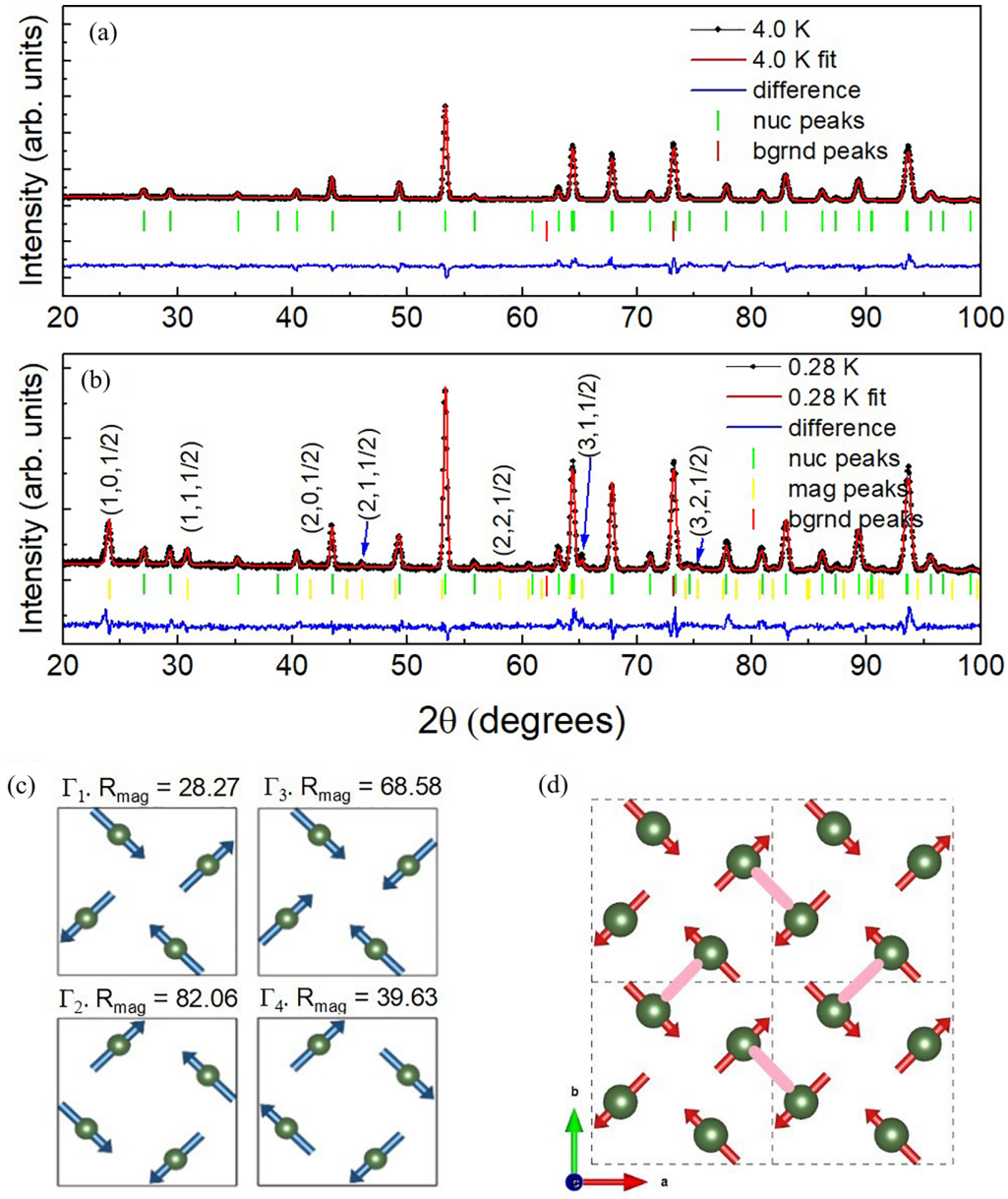

FIG. 9. (a) The neutron powder diffraction pattern collected at 4 K (above T_N). The best Rietveld refinement result is superimposed on the data. The nuclear Bragg peaks from the sample and the background are indicated by green and red ticks, respectively, and the difference curve is shown below the Bragg peaks. (b) The neutron powder diffraction pattern collected at 0.28 K (below T_N). The best Rietveld refinement result, which now includes a magnetic phase, is again superimposed on the data. The magnetic Bragg peaks are denoted by the yellow ticks. (c) Schematics of the in-plane spin structures for the Γ_1 to Γ_4 models. The R_{mag} values for the best refinements (which include out-of-plane components when allowed by symmetry) using each of these models are also shown. (d) The spin configuration of the Γ_1 magnetic structure realized by $Er_2Be_2SiO_7$ below T_N, with the dimer bonds shown in pink. The moments have a magnitude of $2.47(3)\,\mu_B$, and each square plaquette consists of two moments pointing into it and two pointing out.

confirmed by performing a Rietveld refinement using the FULLPROF software suite [73] on a diffraction pattern collected above T_N at 4 K. The data and the refinement results are shown in Fig. 9(a). The obtained lattice parameters, $a = 7.262$ Å and $c = 4.744$ Å, agree well with the XRD results discussed above. No evidence of a structural transition between 4 K and 300 K is found.

A second neutron diffraction pattern was measured well below T_N at 0.28 K. The nuclear phase was first refined using the parameters obtained from the 4 K fit as a starting point, and no significant changes to the crystal structure were identified. Several additional Bragg peaks are visible in the low-temperature data, and they could be indexed to a magnetic propagation vector of $\vec{k} = (0, 0, 0.5)$. Since there is only one SSL plane per chemical unit cell for the $R_2Be_2SiO_7$ family, this implies that the dominant interplane coupling is antiferromagnetic (AFM). With the magnetic propagation vector established, the software package SARAh [87] was used to identify all five irreducible representations (IRs) in Kovalev's notation [88] allowed by symmetry. The Γ_1-Γ_4 IRs correspond

to spin states with AFM dimers, while the Γ_5 IR has ferromagnetic (FM) dimers. The Γ_1 and Γ_3 magnetic structures have their moments confined to the local directions perpendicular to the dimer bonds in the *ab* plane, with Γ_1 and Γ_3 consisting of two different square plaquette spin configurations. The Γ_2 and Γ_4 magnetic structures can have in-plane moments parallel to the dimer bonds, out-of-plane moments, or some combination of both. There are two main differences between them. First, the Γ_4 in-plane moments form a magnetic state with a definite handedness, but this is not true for Γ_2. Second, in a given SSL plane the *c*-axis moments are parallel for the Γ_2 structure, while they are antiparallel for the two dimer sublattices of the Γ_4 configuration. Schematics for the in-plane moment configurations of the Γ_1 to Γ_4 magnetic structures are shown in Fig. 9(c).

For $Er_2Be_2SiO_7$, the negative Curie-Weiss temperatures identified above suggest that its low-temperature ground state consists of AFM dimers, and therefore the most likely candidates are the Γ_1-Γ_4 magnetic structures. To test this hypothesis, we performed systematic Rietveld refinements using the 0.28 K NPD data and the calculated magnetic diffraction patterns from each of the IRs in turn. Indeed, we find the largest $R_{\rm mag} = 141.7$ for the Γ_5 model with the FM dimers. The fit quality improves substantially for all four AFM dimer models as shown in Fig. 9(c), but we find the best agreement ($R_{\rm mag} = 28.27$) for the Γ_1 IR. Our Γ_1 magnetic structure refinement returns an ordered moment value of 2.47(3) μ_B and indicates that all the Er moments point along the normal to their local mirror planes. A schematic of the refined magnetic structure viewed along the crystallographic *c* axis is shown in Fig. 9(d).

D. Magnetic phase diagrams

We collected a variety of bulk characterization data with the applied magnetic field along the high-symmetry directions [001], [110], and [100] to explore the possibility of field-induced phase transitions and to establish H-T magnetic phase diagrams. DC magnetization M vs field H is shown at selected temperatures for these three high-symmetry directions in Figs. 10(a)–10(c). The first derivative dM/dH is also shown on these same panels. Although magnetization plateaus are often observed in SSL systems, there is no evidence for them in these data. The in-plane field dependence of both M and dM/dH appears to be quite simple, with only one abrupt slope change in the 0.4 K magnetization data around 0.3–0.4 T corresponding to a large peak in dM/dH. This behavior is indicative of a single metamagnetic transition from the zero-field ground state established above to the field-polarized phase. The real part of the AC susceptibility, plotted in Figs. 10(e) and 10(f), shows that no additional features appear down to 30 mK.

On the other hand, the $H \parallel [001]$ data appear to be more interesting. Aside from clear evidence in the 0.4 K magnetization data for a ∼1.1 T phase transition to a field-polarized state, there is at least one lower-field peak in dM/dH as shown in Fig. 10(a). Furthermore, the AC susceptibility data presented in Fig. 10(d) reveal that the H-T phase diagram becomes more complex when the temperature is decreased below 0.4 K, as an additional peak appears in the data at an intermediate field. This feature may correspond to a third phase transition. The transition to the field-polarized phase occurs at a slightly lower field of 0.8 T in these data only, which is likely due to a slight sample misalignment.

Complementary heat capacity data with the field applied along the same three high-symmetry directions is shown in Figs. 10(g)–10(i). All three datasets have the same general behavior, with clear λ anomalies indicative of low-temperature magnetic order in the lower-field range and broader features characteristic of the field-polarized phase in the higher-field regime. As expected for the zero-field antiferromagnetic state, its ordering temperature is suppressed with increasing field applied along any direction. The field evolution of the magnetic phase transition is extremely anisotropic for in-plane vs out-of-plane fields, with a much larger field required to reach saturation for $H \parallel [001]$.

Figure 11 summarizes the bulk characterization results for the three high-symmetry directions. These H-T phase diagrams were constructed from a combination of the heat capacity data (λ anomaly temperature), the real part of the AC susceptibility (peak fields), and dM/dH (peak fields). As described above, the phase diagrams for the two in-plane field directions are nearly indistinguishable and consist of a single metamagnetic transition from the low-field Γ_1 antiferromagnetic ground state to a field-polarized phase [see Figs. 5(b) and 5(c) for schematics of the high-field spin structures]. The phase diagram for $H \parallel [001]$ is more complex, as we have identified two intermediate field-induced states.

To investigate the microscopic origin of these phases in more detail, we performed a single-crystal neutron diffraction experiment with the magnetic field applied along the [001] direction. This was a challenging measurement due to the low-field magnetic propagation vector of $\vec{k} = (0, 0, 0.5)$, which can only be probed with this field direction using a horizontal-field cryomagnet or a vertical-field cryomagnet with out-of-plane detector geometry. We performed this experiment on DEMAND since it offers the latter combination, although very few magnetic Bragg peaks could be measured in each phase due to the limited vertical acceptance of the cryomagnet.

The main results of the neutron diffraction experiment are shown in Fig. 12. While we identified $\vec{k} = 0$ and $\vec{k} = (0, 0, 0.5)$ Bragg peaks in these measurements, no peaks indicative of additional magnetic propagation vectors were found at any applied field. Here we present the field evolution of the (3,1,0) and (3,1,0.5) Bragg peak integrated intensities at a fixed temperature of 0.28 K. There are three different field regimes. For the lowest fields, both the (3,1,0) and (3,1,0.5) integrated intensities are roughly constant. For intermediate fields, the (3,1,0.5) peak and the (3,1,0) peak intensities show a large decrease and increase, respectively. For the highest fields, the (3,1,0.5) peak intensity is completely suppressed, while the (3,1,0) peak shows another modest intensity increase. The field evolution of the (3,1,0) peak tracks the 0.4 K magnetization data well, which shows that it is an effective probe of the net moment along the *c* axis. These results indicate that one of the intermediate phases corresponds to a $2\vec{k}$ structure, with the in-plane and out-of-plane moment components giving rise to the $\vec{k} = (0, 0, 0.5)$ and $\vec{k} = 0$ magnetic

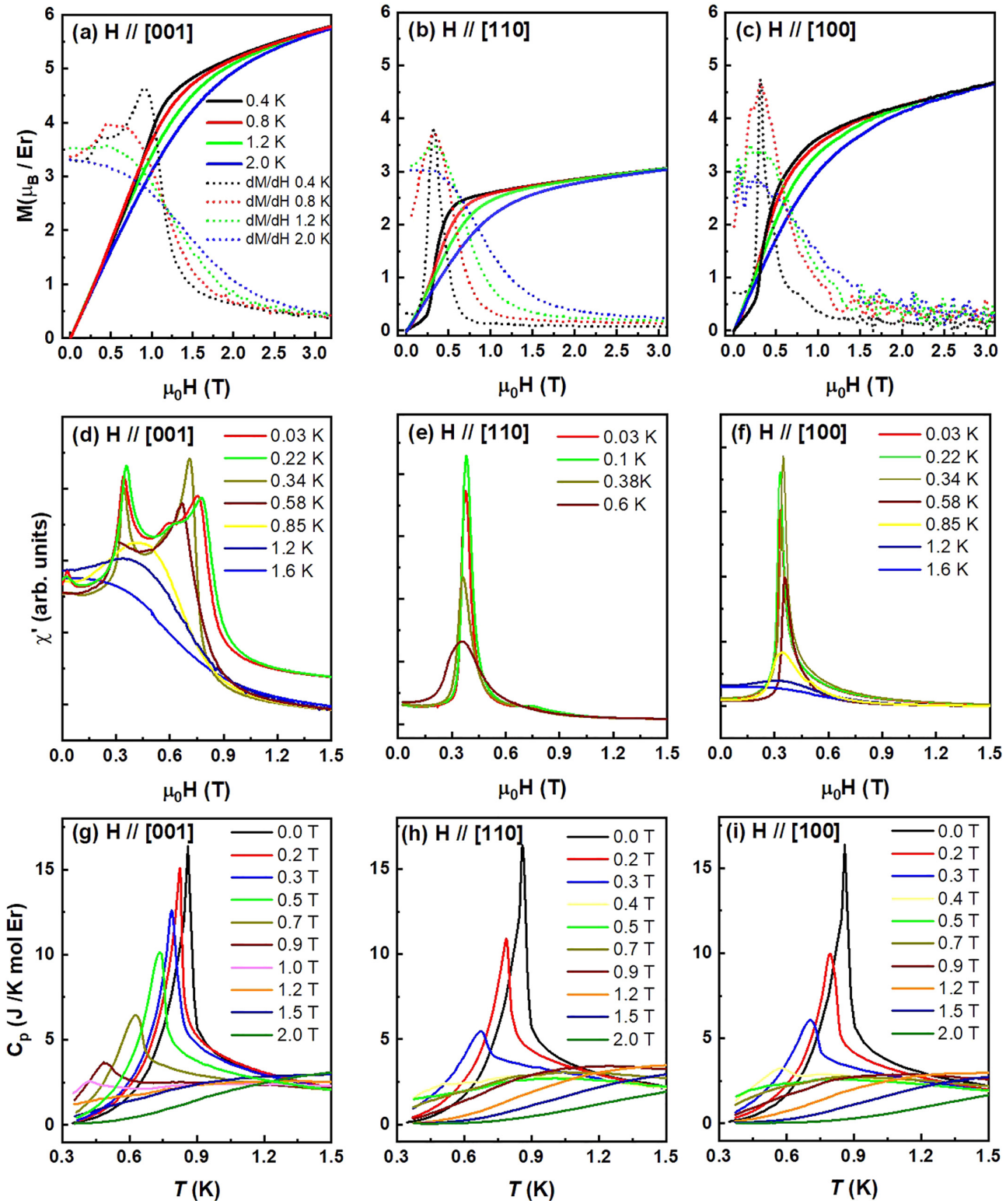

FIG. 10. (a–c) DC magnetization and dM/dH vs H for applied magnetic fields along the [001], [110], and [100] directions at select temperatures. While only a single peak in dM/dH indicative of one metamagnetic phase transition is visible in the low-T in-plane field data, there are at least two dM/dH peaks when $H \parallel [001]$. (d–f) The real component of the AC susceptibility χ' vs H. While the results generally agree with the DC magnetization, there is an extra peak in the lowest-T $H \parallel [001]$ χ' data, which suggests that the H-T phase diagram becomes more complex below 0.4 K. The appearance of peaks in the χ' data at slightly lower fields, compared to the magnetization results, is likely due to a slight sample misalignment. (g–i) Heat capacity data C_p vs T for all three field orientations. In each case, the zero-field λ anomaly indicative of magnetic order is suppressed with increasing field and replaced by a broad hump in the higher field range signifying the field-polarized phase regime. The onset of the polarized phase occurs at a much higher field for $H \parallel [001]$ due to the significant magnetic anisotropy of this system.

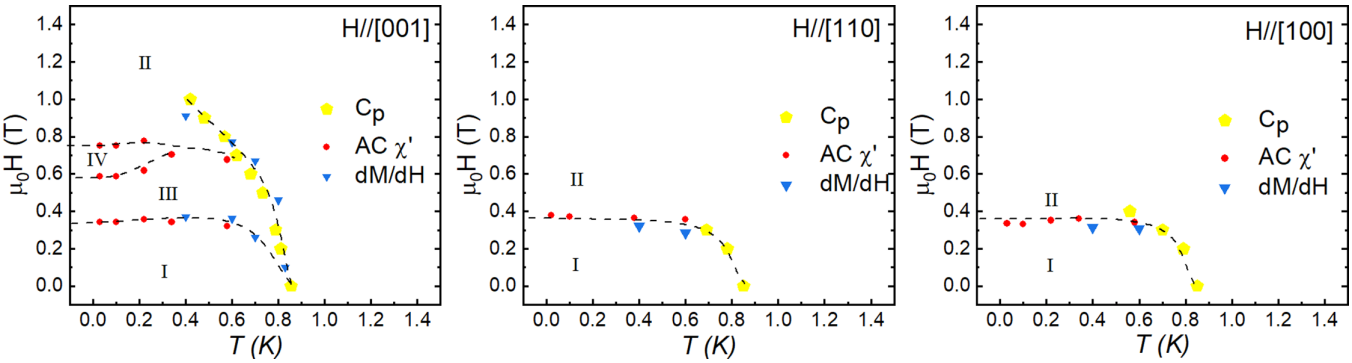

FIG. 11. H-T phase diagrams for $Er_2Be_2SiO_7$ with $H \parallel [001]$, $H \parallel [110]$, and $H \parallel [100]$. Dashed lines are drawn as guides to the eye. The in-plane field behavior is quite simple and consists of only phase I and phase II, which correspond to the Γ_1 magnetic structure and the field-polarized state. There are two additional phases for $H \parallel [001]$ found at intermediate field ranges between phase I and II. Single-crystal neutron diffraction suggests that phase III is a $2\vec{k}$ magnetic structure corresponding to a field-induced canting of the moments towards the c axis, while the nature of phase IV remains unknown.

propagation vectors, respectively. The onset of the polarized phase corresponds to the disappearance of the (3,1,0.5) peak and hence the complete suppression of the in-plane moment component. There appears to be a weak energy barrier that must be overcome by the magnetic field to reach the $2\vec{k}$ state since the (3,1,0.5) peak intensity does not decrease immediately after the field is applied. This behavior provides further evidence that the Er moments in this system have quasi-XY rather than true XY magnetic anisotropy. Finally, we note that there is no evidence for the second intermediate-field phase in this data, which may be due to the elevated base temperature as compared to the AC susceptibility measurement.

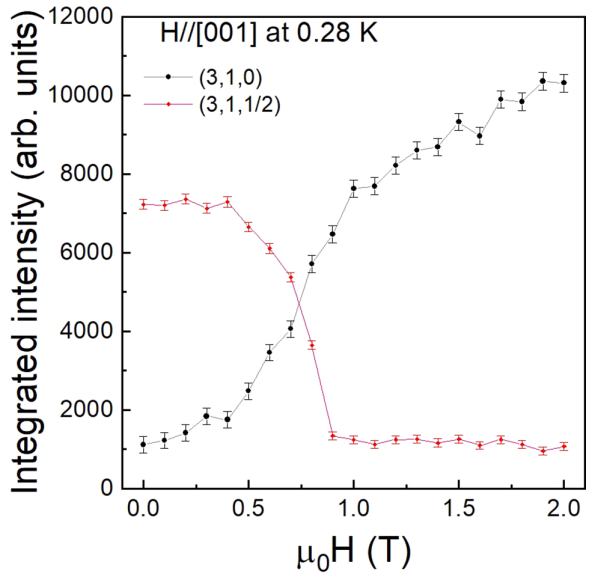

FIG. 12. Field dependence of the integrated intensity for the (3,1,0) and (3,1,0.5) Bragg peaks. While the (3,1,0.5) integrated intensity drops sharply between 0.4 and 1 T, the (3,1,0) integrated intensity tracks the field dependence of the DC magnetization at comparable temperatures quite well. The field dependence of these two peaks matches expectations for a field-induced canting of the moments towards the c axis that cannot proceed until a small energy barrier due to the magnetic anisotropy of the system is overcome first.

IV. CONCLUSIONS

We investigated the structural and magnetic properties of both polycrystalline and single-crystal samples of the Shastry-Sutherland lattice system $Er_2Be_2SiO_7$ using a variety of bulk characterization and scattering techniques. This material crystallizes in the tetragonal $P\text{-}42_1m$ space group (113) over a wide temperature range from 0.28 K to 300 K. The Er moments have a quasi-XY magnetic anisotropy with a small preference to lie along the normal to their local mirror plane, which corresponds to the crystallographic [110] or [1-10] direction for the two orthogonal dimer sublattices. Inelastic neutron scattering data show that the $J_{\text{eff}} = 1/2$ model is not appropriate for this system due to a low-lying crystal field level, and it was also used to establish some probable crystal field parameters for this material.

$Er_2Be_2SiO_7$ exhibits long-range noncollinear magnetic order below $T_N = 0.841$ K. The Shastry-Sutherland planes of the Γ_1 structure consist of antiferromagnetic dimers with in-plane moments perpendicular to the dimer bonds and square plaquettes with two moments pointing in and two moments pointing out of them. The $\vec{k} = (0, 0, 0.5)$ magnetic propagation vector also ensures that there is antiferromagnetic coupling between the Shastry-Sutherland planes. A modest in-plane magnetic field ~0.4 T induces a magnetic transition from the Γ_1 magnetic structure to a field-polarized phase. An $H \parallel [001]$ field generates a more complicated H-T phase diagram with at least two intermediate field states between the Γ_1 and field-polarized phases. One intermediate phase has a $2\vec{k}$ magnetic structure corresponding to a gradual canting of the moments towards the c axis with increasing field, while the nature of the second intermediate phase remains unknown. The microscopic origins of the field-induced phases elucidated here are consistent with expectations for the behavior of classical, anisotropic moments.

Despite the conventional magnetic properties of $Er_2Be_2SiO_7$, we expect our work to motivate comprehensive magnetism studies of other isostructural $R_2Be_2SiO_7$ and $R_2Be_2GeO_7$ family members. There is a strong likelihood that the rare-earth-based Shastry-Sutherland planes, combined with specific magnetic anisotropies and insulating behavior, will generate exotic zero-field magnetic ground states

and field-induced magnetization plateaus for many family members that can be readily compared to theoretical predictions of the beyond-Heisenberg Shastry-Sutherland model. In fact, both features have been identified in recent work on a subset of these materials [70–72].

ACKNOWLEDGMENTS

Research at the University of Tennessee is supported by the National Science Foundation, Division of Materials Research under Award No. NSF-DMR-2003117. The work at Michigan State University is supported by the U.S.DOE-BES under Contract No. DE-SC0023648. The work performed at NHMFL is supported by the NSF Cooperative Agreement No. DMR-1644779 and the State of Florida. A portion of this research used resources at the Spallation Neutron Source and the High Flux Isotope Reactor, which are DOE Office of Science User Facilities operated by Oak Ridge National Laboratory (ORNL). A portion of the research at ORNL was supported by the DOE, Office of Science, Office of Advanced Scientific Computing Research (Contract No. ERKJ387), and Office of Basic Energy Sciences (Award No. KC0402020 under Contract No. DE-AC05-000R22725).

[1] A. P. Ramirez, Strongly geometrically frustrated magnets, Annu. Rev. Mater. Sci. **24**, 453 (1994).
[2] J. E. Greedan, Geometrically frustrated magnetic materials, J. Mater. Chem. **11**, 37 (2001).
[3] R. Moessner and A. P. Ramirez, Geometrical frustration, Phys. Today **59**, 24 (2006).
[4] I. Mirebeau and S. Petit, Magnetic frustration probed by inelastic neutron scattering: Recent examples, J. Magn. Magn. Mater. **350**, 209 (2014).
[5] L. Balents, Spin liquids in frustrated magnets, Nature (London) **464**, 199 (2010).
[6] M. R. Norman, Colloquium: Herbertsmithite and the search for the quantum spin liquid, Rev. Mod. Phys. **88**, 041002 (2016).
[7] L. Savary and L. Balents, Quantum spin liquids: A review, Rep. Prog. Phys. **80**, 016502 (2017).
[8] Y. Zhou, K. Kanoda, and T. K. Ng, Quantum spin liquid states, Rev. Mod. Phys. **89**, 025003 (2017).
[9] J. Knolle and R. Moessner, A field guide to spin liquids, Annu. Rev. Condens. Matter Phys. **10**, 451 (2019).
[10] H. Takagi, T. Takayama, G. Jackeli, G. Khaliullin, and S. E. Nagler, Concept and realization of Kitaev quantum spin liquids, Nat. Rev. Phys. **1**, 264 (2019).
[11] J. Wen, S. L. Yu, S. Li, W. Yu, and J. X. Li, Experimental identification of quantum spin liquids, npj Quantum Mater. **4**, 12 (2019).
[12] C. Broholm, R. J. Cava, S. A. Kivelson, D. G. Nocera, M. R. Norman, and T. Senthil, Quantum spin liquids, Science **367**, eaay0668 (2020).
[13] J. R. Chamorro, T. M. McQueen, and T. T. Tran, Chemistry of quantum spin liquids, Chem. Rev. **121**, 2898 (2021).
[14] J.-X. Yin, B. Lian, and M. Z. Hasan, Topological kagome magnets and superconductors, Nature (London) **612**, 647 (2022).
[15] J. E. Greedan, Frustrated rare earth magnetism: Spin glasses, spin liquids and spin ices in pyrochlore oxides, J. Alloys Compd. **408–412**, 444 (2006).
[16] J. S. Gardner, M. J. P. Gingras, and J. E. Greedan, Magnetic pyrochlore oxides, Rev. Mod. Phys. **82**, 53 (2010).
[17] O. A. Starykh, Unusual ordered phases of highly frustrated magnets: A review, Rep. Prog. Phys. **78**, 052502 (2015).
[18] B. Sriram Shastry and B. Sutherland, Exact ground state of a quantum mechanical antiferromagnet, Physica B+C **108**, 1069 (1981).
[19] S. Miyahara and K. Ueda, Exact dimer ground state of the two dimensional Heisenberg spin system $SrCu_2(BO_3)_2$, Phys. Rev. Lett. **82**, 3701 (1999).
[20] H. Kageyama, K. Yoshimura, R. Stern, N. V. Mushnikov, K. Onizuka, M. Kato, K. Kosuge, C. P. Slichter, T. Goto, and Y. Ueda, Exact dimer ground state and quantized magnetization plateaus in the two-dimensional spin system $SrCu_2(BO_3)_2$, Phys. Rev. Lett. **82**, 3168 (1999).
[21] J. Guo, G. Sun, B. Zhao, L. Wang, W. Hong, V. A. Sidorov, N. Ma, Q. Wu, S. Li, Z. Y. Meng, A. W. Sandvik, and L. Sun, Quantum phases of $SrCu_2(BO_3)_2$ from high-pressure thermodynamics, Phys. Rev. Lett. **124**, 206602 (2020).
[22] T. Sakurai, M. Tomoo, S. Okubo, H. Ohta, K. Kudo, and Y. Koike, High-field and high-pressure ESR measurements of $SrCu_2(BO_3)_2$, J. Phys.: Conf. Ser. **150**, 042171 (2009).
[23] S. Haravifard, D. Graf, A. E. Feiguin, C. D. Batista, J. C. Lang, D. M. Silevitch, G. Srajer, B. D. Gaulin, H. A. Dabkowska, and T. F. Rosenbaum, Crystallization of spin superlattices with pressure and field in the layered magnet $SrCu_2(BO_3)_2$, Nat. Commun. **7**, 11956 (2016).
[24] J. Yang, A. W. Sandvik, and L. Wang, Quantum criticality and spin liquid phase in the Shastry-Sutherland model, Phys. Rev. B **105**, L060409 (2022).
[25] L. Wang, Y. Zhang, and A. W. Sandvik, Quantum spin liquid phase in the Shastry-Sutherland model detected by an improved level spectroscopic method, Chin. Phys. Lett. **39**, 077502 (2022).
[26] S. Miyahara and K. Ueda, The magnetization plateaus of $SrCu_2(BO_3)_2$, Phys. B: Condens. Matter **281–282**, 661 (2000).
[27] H. Kageyama, M. Nishi, N. Aso, K. Onizuka, T. Yosihama, K. Nukui, K. Kodama, K. Kakurai, and Y. Ueda, Direct evidence for the localized single-triplet excitations and the dispersive multitriplet excitations in $SrCu_2(BO_3)_2$, Phys. Rev. Lett. **84**, 5876 (2000).
[28] S. Miyahara and K. Ueda, Superstructures at magnetization plateaus in $SrCu_2(BO_3)_2$, Phys. Rev. B **61**, 3417 (2000).
[29] S. Sebastian, N. Harrison, P. Sengupta, C. Batista, S. Francoual, E. Palm, T. Murphy, N. Marcano, H. Dabkowska, and B. Gaulin, Fractalization drives crystalline states in a frustrated spin system, Proc. Natl. Acad. Sci. USA **105**, 20157 (2008).
[30] S. Ji, C. Song, J. Koo, K.-B. Lee, Y. J. Park, J. Y. Kim, J.-H. Park, H. J. Shin, J. S. Rhyee, B. H. Oh, and B. K. Cho, Interference of magnetic and anisotropic tensor susceptibility reflections in resonant x-ray scattering of GdB_4, Phys. Rev. Lett. **91**, 257205 (2003).
[31] R. Watanuki, G. Sato, K. Suzuki, M. Ishihara, T. Yanagisawa, Y. Nemoto, and T. Goto, Geometrical quadrupolar frustration in DyB_4, J. Phys. Soc. Jpn. **74**, 2169 (2005).

[32] G. A. Wigger, E. Felder, R. Monnier, H. R. Ott, L. Pham, and Z. Fisk, Low-temperature phase transitions in the induced-moment system PrB_4, Phys. Rev. B **72**, 014419 (2005).

[33] S. Yoshii, T. Yamamoto, M. Hagiwara, A. Shigekawa, S. Michimura, F. Iga, T. Takabatake, and K. Kindo, High-field magnetization of TmB_4, J. Phys.: Conf. Ser. **51**, 59 (2006).

[34] S. Michimura, A. Shigekawa, F. Iga, M. Sera, T. Takabatake, K. Ohoyama, and Y. Okabe, Magnetic frustrations in the Shastry–Sutherland system ErB_4, Phys. B: Condens. Matter **378–380**, 596 (2006).

[35] T. Matsumura, D. Okuyama, and Y. Murakami, Non-collinear magnetic structure of TbB_4, J. Phys. Soc. Jpn. **76**, 015001 (2007).

[36] D. Okuyama, T. Matsumura, K. Iwasa, and Y. Murakami, Magnetic phase transition in HoB_4 studied by neutron diffraction, J. Magn. Magn. Mater. **310**, e152 (2007).

[37] J. Y. Kim, N. H. Sung, B. Y. Kang, M. S. Kim, B. K. Cho, and J.-S. Rhyee, Magnetic anisotropy and magnon gap state of SmB_4 single crystal, J. Appl. Phys. **107**, 09E111 (2010).

[38] H. Yamauchi, N. Metoki, R. Watanuki, K. Suzuki, H. Fukazawa, S. Chi, and J. A. Fernandez-Baca, Magnetic structure and quadrupolar order parameter driven by geometrical frustration effect in NdB_4, J. Phys. Soc. Jpn. **86**, 044705 (2017).

[39] Z. Fisk, M. Maple, D. Johnston, and L. Woolf, Multiple phase transitions in rare earth tetraborides at low temperature, Solid State Commun. **39**, 1189 (1981).

[40] J. Gianduzzo, R. Georges, B. Chevalier, J. Etourneau, P. Hagenmuller, G. Will, and W. Schäfer, Anisotropy and magnetic phase transitions in the rare earth tetraborides TbB_4, HoB_4 and ErB_4, J. Less-Common Met. **82**, 29 (1981).

[41] G. Will, W. Schäfer, F. Pfeiffer, F. Elf, and J. Etourneau, Neutron diffraction studies of TbB_4 and ErB_4, J. Less-Common Met. **82**, 349 (1981).

[42] F. Iga, A. Shigekawa, Y. Hasegawa, S. Michimura, T. Takabatake, S. Yoshii, T. Yamamoto, M. Hagiwara, and K. Kindo, Highly anisotropic magnetic phase diagram of a 2-dimensional orthogonal dimer system TmB_4, J. Magn. Magn. Mater. **310**, e443 (2007).

[43] D. Okuyama, T. Matsumura, T. Mouri, N. Ishikawa, K. Ohoyama, H. Hiraka, H. Nakao, K. Iwasa, and Y. Murakami, Competition of magnetic and quadrupolar order parameters in HoB_4, J. Phys. Soc. Jpn. **77**, 044709 (2008).

[44] H. Sim, S. Lee, K.-P. Hong, J. Jeong, J. R. Zhang, T. Kamiyama, D. T. Adroja, C. A. Murray, S. P. Thompson, F. Iga, S. Ji, D. Khomskii, and J.-G. Park, Spontaneous structural distortion of the metallic Shastry-Sutherland system DyB_4 by quadrupole-spin-lattice coupling, Phys. Rev. B **94**, 195128 (2016).

[45] J. A. Blanco, P. J. Brown, A. Stunault, K. Katsumata, F. Iga, and S. Michimura, Magnetic structure of GdB_4 from spherical neutron polarimetry, Phys. Rev. B **73**, 212411 (2006).

[46] F. Hulliger, On new Mo_2FeB_2-type representatives Ln_2Rh_2In, J. Alloys Compd. **221**, L11 (1995).

[47] M. Giovannini, H. Michor, E. Bauer, G. Hilscher, P. Rogl, and R. Ferro, Structural chemistry, magnetism and thermodynamic properties of R_2Pd_2In, J. Alloys Compd. **280**, 26 (1998).

[48] R. Kraft, T. Fickenscher, G. Kotzyba, R.-D. Hoffmann, and R. Pöttgen, Intermetallic rare earth (*RE*) magnesium compounds *RE*PdMg and RE_2Pd_2Mg, Intermetallics **11**, 111 (2003).

[49] V. I. Zaremba, D. Kaczorowski, G. P. Nychyporuk, U. C. Rodewald, and R. Pöttgen, Structure and physical properties of RE_2Ge_2In (*RE* = La, Ce, Pr, Nd), Solid State Sci. **6**, 1301 (2004).

[50] S. Rayaprol, A. Doğan, and R. Pöttgen, Magnetic properties and specific heat studies of RE_2Pd_2Cd (RE = La, Ce, Nd), J. Phys.: Condens. Matter **18**, 5473 (2006).

[51] P. Kumar, N. K. Singh, K. G. Suresh, and A. K. Nigam, Magnetocaloric and magnetotransport properties of R_2Ni_2Sn compounds (R = Ce, Nd, Sm, Gd, and Tb), Phys. Rev. B **77**, 184411 (2008).

[52] F. M. Schappacher, W. Hermes, and R. Pöttgen, Structure and magnetic properties of RE_2Cu_2Cd, J. Solid State Chem. **182**, 265 (2009).

[53] K. V. Shah, P. Bonville, P. Manfrinetti, F. Wrubl, and S. K. Dhar, The $Yb_2Al_{1-x}Mg_xSi_2$ series from a spin fluctuation ($x = 0$) to a magnetically ordered ground state ($x = 1$), J. Phys.: Condens. Matter **21**, 176001 (2009).

[54] N.-T. Suen, P. H. Tobash, and S. Bobev, Synthesis, structural characterization and magnetic properties of RE_2MgGe_2 (*RE* = rare-earth metal), J. Solid State Chem. **184**, 2941 (2011).

[55] Y. Shimura, T. Sakakibara, K. Iwakawa, K. Sugiyama, and Y. Ōnuki, Low temperature magnetization of Yb_2Pt_2Pb with the Shastry–Sutherland type lattice and a high-rank multipole interaction, J. Phys. Soc. Jpn. **81**, 103601 (2012).

[56] W. Miiller, L. S. Wu, M. S. Kim, T. Orvis, J. W. Simonson, M. Gamza, D. M. McNally, C. S. Nelson, G. Ehlers, A. Podlesnyak *et al.*, Magnetic structure of Yb_2Pt_2Pb: Ising moments on the Shastry-Sutherland lattice, Phys. Rev. B **93**, 104419 (2016).

[57] L. S. Wu, W. J. Gannon, I. A. Zaliznyak, A. M. Tsvelik, M. Brockmann, J.-S. Caux, M. S. Kim, Y. Qiu, J. R. D. Copley, G. Ehlers, A. Podlesnyak, and M. C. Aronson, Orbital-exchange and fractional quantum number excitations in an f-electron metal Yb_2Pt_2Pb, Science **352**, 1206 (2016).

[58] W. J. Gannon, K. Chen, M. Sundermann, F. Strigari, Y. Utsumi, K.-D. Tsuei, J.-P. Rueff, P. Bencok, A. Tanaka, A. Severing, and M. C. Aronson, Intermediate valence in single crystalline Yb_2Si_2Al, Phys. Rev. B **98**, 075101 (2018).

[59] W. J. Gannon, I. A. Zaliznyak, L. S. Wu, A. E. Feiguin, A. M. Tsvelik, F. Demmel, Y. Qiu, J. R. D. Copley, M. S. Kim, and M. C. Aronson, Spinon confinement and a sharp longitudinal mode in Yb_2Pt_2Pb in magnetic fields, Nat. Commun. **10**, 1123 (2019).

[60] M. Wakeshima, N. Taira, Y. Hinatsu, A. Tobo, K. Ohoyama, and Y. Yamaguchi, Specific heat and neutron diffraction study on quaternary sulfides $BaNd_2CoS_5$ and $BaNd_2ZnS_5$, J. Solid State Chem. **174**, 159 (2003).

[61] T. Ozawa, T. Taniguchi, Y. Kawaji, S. Mizusaki, Y. Nagata, Y. Noro, H. Samata, H. Mitamura, and S. Takayanagi, Magnetization and specific heat measurement of the Shastry–Sutherland lattice compounds: Ln_2BaPdO_5 (Ln = La, Pr, Nd, Sm, Eu, Gd, Dy, Ho), J. Alloys Compd. **448**, 96 (2008).

[62] Y. Ishii, J. Chen, H. K. Yoshida, M. Oda, A. D. Christianson, and K. Yamaura, High-pressure synthesis, crystal structure, and magnetic properties of the Shastry-Sutherland-lattice oxides $BaLn_2ZnO_5$ (Ln = Pr, Sm, Eu), J. Solid State Chem. **289**, 121489 (2020).

[63] Y. Ishii, G. Sala, M. B. Stone, V. O. Garlea, S. Calder, J. Chen, H. K. Yoshida, S. Fukuoka, J. Yan, C. R. Dela Cruz *et al.*, Magnetic properties of the Shastry-Sutherland lattice material $BaNd_2ZnS_5$, Phys. Rev. Mater. **5**, 064418 (2021).

[64] B. R. Billingsley, M. Marshall, Z. Shu, H. Cao, and T. Kong, Single crystal synthesis and magnetic properties of a Shastry-Sutherland lattice compound $BaNd_2ZnS_5$, Phys. Rev. Mater. **6**, 104403 (2022).

[65] M. Marshall, B. R. Billingsley, X. Bai, Q. Ma, T. Kong, and H. Cao, Field-induced partial disorder in a Shastry-Sutherland lattice, Nat. Commun. **14**, 3641 (2023).

[66] C. M. Pasco, B. K. Rai, M. Frontzek, G. Sala, M. B. Stone, B. C. Chakoumakos, V. O. Garlea, A. D. Christianson, and A. F. May, Anisotropic magnetism of the Shastry-Sutherland lattice material $BaNd_2PtO_5$, Phys. Rev. Mater. **7**, 074407 (2023).

[67] M. Ashtar, Y. Bai, L. Xu, Z. Wan, Z. Wei, Y. Liu, M. A. Marwat, and Z. Tian, Structure and magnetic properties of melilite-type compounds $RE_2Be_2GeO_7$ (RE = Pr, Nd, Gd–Yb) with rare-earth ions on Shastry–Sutherland lattice, Inorg. Chem. **60**, 3626 (2021).

[68] A. Brassington, Q. Huang, A. A. Aczel, and H. D. Zhou, Synthesis and magnetic properties of the Shastry-Sutherland family $R_2Be_2SiO_7$ (R = Nd,Sm,Gd-Yb), Phys. Rev. Mater. **8**, 014005 (2024).

[69] F. Song, Y. Gao, A. Liu, L. Xu, M. Ashtar, Z. Tian, and S. Yuan, Tunable magnetism and large inverse magnetocaloric effect in Shastry-Sutherland compounds $Tb_2Be_2Si_{1-x}Ge_xO_7$ ($0 \leqslant x \leqslant 1$), J. Alloys Compd. **960**, 170657 (2023).

[70] A. Liu, F. Song, Y. Cao, H. Ge, H. Bu, J. Zhou, Y. Qin, Q. Zeng, J. Li, L. Ling *et al.*, Distinct magnetic ground states in Shastry-Sutherland lattice materials: $Pr_2Be_2GeO_7$ versus $Nd_2Be_2GeO_7$, Phys. Rev. B **109**, 184413 (2024).

[71] L. Yadav, A. Rufino, B. R., C. R. Dela Cruz, A. Kolesnikov, O. Garlea, G. D, F. Mila, and S. Haravifard, Observation of unprecedented fractional magnetization plateaus in a new Shastry-Sutherland Ising compound, arXiv:2405.12405.

[72] M. Pula, S. Sharma, J. Gautreau, K. P. Sajilesh, A. Kanigel, M. D. Frontzek, T. N. Dolling, L. Clark, S. Dunsiger, A. Ghara, and G. M. Luke, Candidate for a quantum spin liquid ground state in the Shastry-Sutherland lattice material $Yb_2Be_2GeO_7$, Phys. Rev. B **110**, 014412 (2024).

[73] J. Rodríguez-Carvajal, Recent advances in magnetic structure determination by neutron powder diffraction, Phys. B: Condens. Matter **192**, 55 (1993).

[74] G. M. Kuz'micheva, V. B. Rybakov, S. A. Kutovoi, V. L. Panyutin, A. Y. Oleinik, and O. G. Plashkarev, Preparation, structure, and properties of new laser crystals $Y_2SiBe_2O_7$ and $Y_2Al(BeB)O_7$, Inorg. Mater. **38**, 60 (2002).

[75] S. Calder, K. An, R. Boehler, C. R. Dela Cruz, M. D. Frontzek, M. Guthrie, B. Haberl, A. Huq, S. A. J. Kimber, J. Liu *et al.*, A suite-level review of the neutron powder diffraction instruments at Oak Ridge National Laboratory, Rev. Sci. Instrum. **89**, 092701 (2018).

[76] G. E. Granroth, A. I. Kolesnikov, T. E. Sherline, J. P. Clancy, K. A. Ross, J. P. C. Ruff, B. D. Gaulin, and S. E. Nagler, SEQUOIA: A newly operating chopper spectrometer at the SNS, J. Phys.: Conf. Ser. **251**, 012058 (2010).

[77] H. Cao, B. C. Chakoumakos, K. M. Andrews, Y. Wu, R. A. Riedel, J. Hodges, W. Zhou, R. Gregory, B. Haberl, J. Molaison, and G. W. Lynn, DEMAND, a dimensional extreme magnetic neutron diffractometer at the High Flux Isotope Reactor, Crystals **9**, 5 (2019).

[78] A. Ochiai, S. Matsuda, Y. Ikeda, Y. Shimizu, S. Toyoshima, H. Aoki, and K. Katoh, Field-induced partially disordered state in Yb_2Pt_2Pb, J. Phys. Soc. Jpn. **80**, 123705 (2011).

[79] M. Hutchings, *Point-Charge Calculations of Energy Levels of Magnetic Ions in Crystalline Electric Fields* (Academic Press, New York, London, 1964), pp. 227–273.

[80] A. Scheie, M. Sanders, J. Krizan, A. D. Christianson, V. O. Garlea, R. J. Cava, and C. Broholm, Crystal field levels and magnetic anisotropy in the kagome compounds $Nd_3Sb_3Mg_2O_{14}$, $Nd_3Sb_3Zn_2O_{14}$, and $Pr_3Sb_3Mg_2O_{14}$, Phys. Rev. B **98**, 134401 (2018).

[81] A. Scheie, *PyCrystalField*: Software for calculation, analysis and fitting of crystal electric field Hamiltonians, J. Appl. Crystallogr. **54**, 356 (2021).

[82] K. W. H. Stevens, Matrix elements and operator equivalents connected with the magnetic properties of rare earth ions, Proc. Phys. Soc. A **65**, 209 (1952).

[83] J. Jensen and A. R. Mackintosh, *Rare Earth Magnetism: Structures and Excitations* (Clarendon Press, Oxford, 1991).

[84] Q. Ma, X. Bai, E. Feng, G. Zhang, and H. Cao, *CrysFieldExplorer*: Rapid optimization of the crystal field Hamiltonian, J. Appl. Crystallogr. **56**, 1229 (2023).

[85] Spectroscopic and magnetic susceptibility analyses of the ^7F_J and $^5D_4$ energy levels of $Tb^{3+}(4f^8)$ in $TbAlO_3$, J. Lumin. **128**, 1271 (2008).

[86] A. Brassington (unpublished).

[87] A. Wills, A new protocol for the determination of magnetic structures using simulated annealing and representational analysis (SARAh), Phys. B: Condens. Matter **276–278**, 680 (2000).

[88] O. Kovalev, *Representations of the Crystallographic Space Groups*, 2nd ed. (Gordon and Breach, Yverdon, 1993).